RSC Advances

ROYAL SOCIETY OF CHEMISTRY

PAPER

View Article Online
View Journal | View Issue

Cite this: *RSC Adv.*, 2025, **15**, 42071

Green synthesized mesoporous silica nanoparticles offer a promising drug delivery system investigated in physiologically relevant 3D microfluidic models

Sahar Porrang,[a] Gulin Baran[a] and Nur Mustafaoglu *[ab]

Mesoporous silica nanoparticles (MSNs) are attractive drug delivery carriers, and green synthesis from biowaste offers an eco-friendly alternative to conventional methods. Unlike previous studies limited to a single precursor, this work systematically compares multiple biosources, including rice husk (RH), wheat husk (WH), wheat stalk (WS), oat husk (OH), oat stalk (OS), and horsetail (HT), and establishes a standardized route to evaluate precursor influence. Among the tested precursors, RH and HT produced the highest purity silica and were selected for MSN synthesis. The resulting MSNs showed well-defined mesoporosity, high surface area, and controlled pore sizes, confirmed by FTIR, XRD, BET, and HR-TEM with pH-responsive Dox release enhanced under acidic conditions. They were biocompatible with HDFs, HUVECs, and U87 cells, while Dox-loaded MSNs exhibited strong anticancer effects against U87 cells at low drug concentration. The second novelty lies in evaluating MSN cellular uptake under physiologically relevant conditions using a microfluidic platform that mimics blood circulation, in contrast to conventional static assays. Cellular uptake was analyzed in 2D cultures and 3D microfluidic models, incorporating both static and dynamic conditions using HUVECs and U87. Notably, the dynamic 3D model, which simulates blood circulation, significantly enhanced MSN uptake by HUVECs and U87 compared to static conditions. These results emphasize the importance of physiological flow in optimizing nanoparticle-based drug delivery. This study introduces a dual innovation by establishing a consistent, multi-biosource approach for green MSN synthesis and validating their drug delivery potential in a realistic dynamic microenvironment, bridging sustainable nanomaterial development with advanced preclinical testing.

Received 19th August 2025
Accepted 16th October 2025

DOI: 10.1039/d5ra06132f

rsc.li/rsc-advances

Introduction

Nanomedicine has made remarkable advances in recent decades, especially in the design of efficient drug delivery systems (DDSs) that enhance therapeutic outcomes while minimizing side effects.[1–3] Among various nanomaterials, mesoporous silica nanoparticles (MSNs) have shown significant promise due to their unique structural and chemical properties, including large surface area, controllable pore structure, high loading capacity, and biocompatibility.[4–8] However, the widespread adoption of MSNs in drug delivery and nanomedicine faces challenges, particularly in scalability. A major limitation is the reliance on expensive and potentially hazardous alkoxysilanes, such as tetraethyl orthosilicate (TEOS), for MSN synthesis.[9–12] TEOS is commercially produced using metallurgical-grade silicon (Si_{mg}) as the raw material. While its synthesis process is well-established, the production of Si_{mg} from silica-rich sources requires a high-temperature (1900 °C) carbothermal reduction process, which is energy-intensive and generates substantial CO_2 emissions.[4,13] Consequently, conventional MSN synthesis is not only costly but also environmentally unsustainable, as the combustion of carbon-based precursors and the energy demand contribute significantly to carbon emission.[4,13] As an alternative, sodium silicate as an affordable and widely available precursor, has been explored for silica-based nanoparticle synthesis.[5,7,14,15] However, its industrial production is also energy-intensive, involving high-temperature melting (1300–1600 °C) of a mixture of high-purity sodium carbonate and quartz sand, leading to further CO_2 emissions.[7,14,15] These challenges highlight the urgent need for innovative, sustainable approaches to MSN synthesis.

However, extracting silica from biowaste sources offers a sustainable, accessible, and cost-effective precursor for MSN synthesis. Several studies have demonstrated the presence of silica in various agricultural biowastes, including rice husk,[16–18] wheat husk,[19–21] horsetail plant,[22,23] oat husk,[24,25] and sugarcane bagasse.[26] Despite ongoing research, a clear understanding of the most effective biowaste sources for silica extraction,

[a]*Molecular Biology, Genetics and Bioengineering Program, Faculty of Engineering and Natural Sciences, Sabanci University, Tuzla, Istanbul, 34956, Türkiye. E-mail: nur.mustafaoglu@sabanciuniv.edu*

[b]*Sabanci University Nanotechnology Research and Application Center (SUNUM), Tuzla, Istanbul, 34956, Türkiye*

especially for nanomedicine application remains lacking. A systematic comparison of these sources is essential to identify the most suitable precursor for MSN synthesis. Since the physicochemical properties of MSNs are influenced by the type of biowaste used, this variability can directly impact their performance as drug carriers. Therefore, comparative evaluation is crucial to develop an efficient and biocompatible MSN-based drug delivery platform.

This study evaluates the potential of several biowaste sources like rice husk (RH), horsetail stalk (HT), wheat husk (WH), wheat stalk (WS), oat husk (OH), and oat stalk (OS), for MSN synthesis, with a focus on nanomedicine applications. A standard method was employed to isolate silica from these biowastes, and the two most promising samples were selected for future investigations. The selected MSNs underwent extensive physicochemical characterizations, including FTIR, XRD, BET surface area analysis, TEM, and zeta potential measurements, to provide detailed insights into their structural, textural, and surface chemical properties and to establish correlations between these features and their performance in drug delivery applications under dynamic cell culture environments. Doxorubicin (Dox), a widely used chemotherapeutic agent, suffers from dose-limiting toxicity and poor selectivity. Encapsulation of Dox within MSN-based carriers can enhance its delivery efficiency and control its release.[27] Dox was used as a model drug to assess MSN drug-loading capacity and encapsulation efficiency. Additionally, the cellular uptake of MSNs as a critical factor influencing drug delivery efficacy was evaluated.[28]

Several recent studies have demonstrated drug delivery applications using biogenic silica source.[5–7,29,30] Andrade *et al.* synthesized rice husk-derived MSNs for doxorubicin delivery, demonstrating high encapsulation efficiency and selective cytotoxicity against colorectal cancer cells.[29] Porrang *et al.* developed biogenic MSNs from rice husk for breast cancer therapy, showing pH-responsive drug release influenced by pore size.[6] Chen *et al.* reported rice husk-derived MSNs functionalized with folic acid and AS1411 aptamer for targeted imaging-assisted delivery of Camptothecin, achieving selective uptake in HeLa cells.[30] However, these works typically relied on a single biosource and were limited to conventional 2D or static models, lacking evaluation under physiologically relevant microfluidic conditions.

To extend beyond previous studies on biogenic MSNs, this work employs biowaste-derived MSNs synthesized from different natural sources to comparatively evaluate their physicochemical and biological features, aiming to identify the most suitable precursor for biomedical use.[31,32] In addition, these MSNs are tested in a dynamic 3D microfluidic system under continuous flow, which mimics physiological blood circulation by incorporating shear stress and constant nutrient exchange. This combination of exploring diverse biowaste precursors with functional testing in a physiologically relevant 3D environment represents a key novelty of this study. This approach also highlights differences in MSN uptake between static and flow conditions, providing a direct comparison between conventional *in vitro* test systems and the *in vivo*-like vascular environment. Such integration of green synthesis of MSNs with microfluidic evaluation represents a novel step forward, bridging the gap between eco-friendly nanomaterial development and advanced preclinical testing platforms.

Materials and method

Materials

Rice husk (RH), horsetail plant (HT), wheat husk (WH), wheat stalk (WS), oat husk (OH), and oat stalk (OS) were obtained from farmers in Iran. Sodium hydroxide (NaOH), hydrochloric acid (HCl), sulfuric acid (H_2SO_4), cetyltrimethylammonium bromide (CTAB), (3-aminopropyl)triethoxysilane (APTES), fluorescein isothiocyanate (FITC), doxorubicin hydrochloride (Dox) were purchased from Sigma-Aldrich (Germany). 3-(4,5-Dimethylthiazol-2-yl)-2,5-diphenyltetrazolium bromide (MTT) and ethanol were obtained from Merck (Germany). Silicone elastomer sylgard® 184 (DOW, Michigan, USA) was used for chip fabrication. Collagen (Sigma-Aldrich, Germany) and fibronectin (Proteintech, USA) were used for coating the chips. Dulbecco's phosphate-buffered saline (DPBS) with (+/+) and without (−/−) calcium and magnesium was purchased from Serena Europe (Germany). Dimethyl sulfoxide (DMSO) was obtained from Genaxxon Bioscience (Germany). Dulbecco's modified eagle medium (DMEM), with 4.5 g L^{-1} glucose was sourced from Gibco (USA). Fetal bovine serum (FBS) was obtained from Serena (Germany), while penicillin-streptomycin was purchased from Bioind Pharma (India). Cell Tracking Red Dye Kit was obtained from Abcam (United Kingdom), DAPI staining solution (10 mM, 2 mL) from Sebra (USA), and ZO-1 monoclonal antibody from Proteintech (USA).

Synthesis of MSNs. The silica extraction process and MSN synthesis protocol were based on previous research,[6,7,33] with several enhancements and the entire process is illustrated in Scheme 1. First, biowaste materials were ground, washed with deionized water to remove dust, and dried in an oven at 90 °C for 3 h. To remove impurities, 5 g of each biowaste sample was acid-washed using 300 mL of 1 M HCl at 100 °C for 3 h while continuous stirring at 600 rpm. The acid-treated samples were then filtered, thoroughly rinsed with distilled water to remove the acid until the pH was neutral, and dried. The samples were then calcinated transferred to at 550 °C for 4 h with a heating rate of 5 °C min^{-1}, yielding white powder. The calcinated materials were labeled as RHA (rice husk ash), HTA (horsetail plant ash), WHA (wheat husk ash), WSA (wheat stalk ash), OHA (oat husk ash), and OSA (oat stalk ash). For MSN synthesis, 1 g of RHA or HTA was dissolved in 18 mL of 2 M NaOH at 80 °C for 3.5 h to prepare a sodium silicate solution (SSS). Separately, 4.8 g of CTAB was dissolved in 100 mL of distilled water at 40 °C for 20 min. The SSS was then added to the CTAB solution, and the pH was adjusted to 11.25. The mixture was stirred for 1 h before being transferred to an oven at 100 °C for 24 h. The resulting white precipitate was washed multiple times with distilled water and calcined at 550 °C for 4 h to remove the surfactant. The MSNs synthesized from RH and HT were designated as RMSN, and HMSN, respectively.

Synthesis of FITC-labeled RMSN. FITC was used to label RMSNs for cellular uptake visualization. First, RMSN's surface

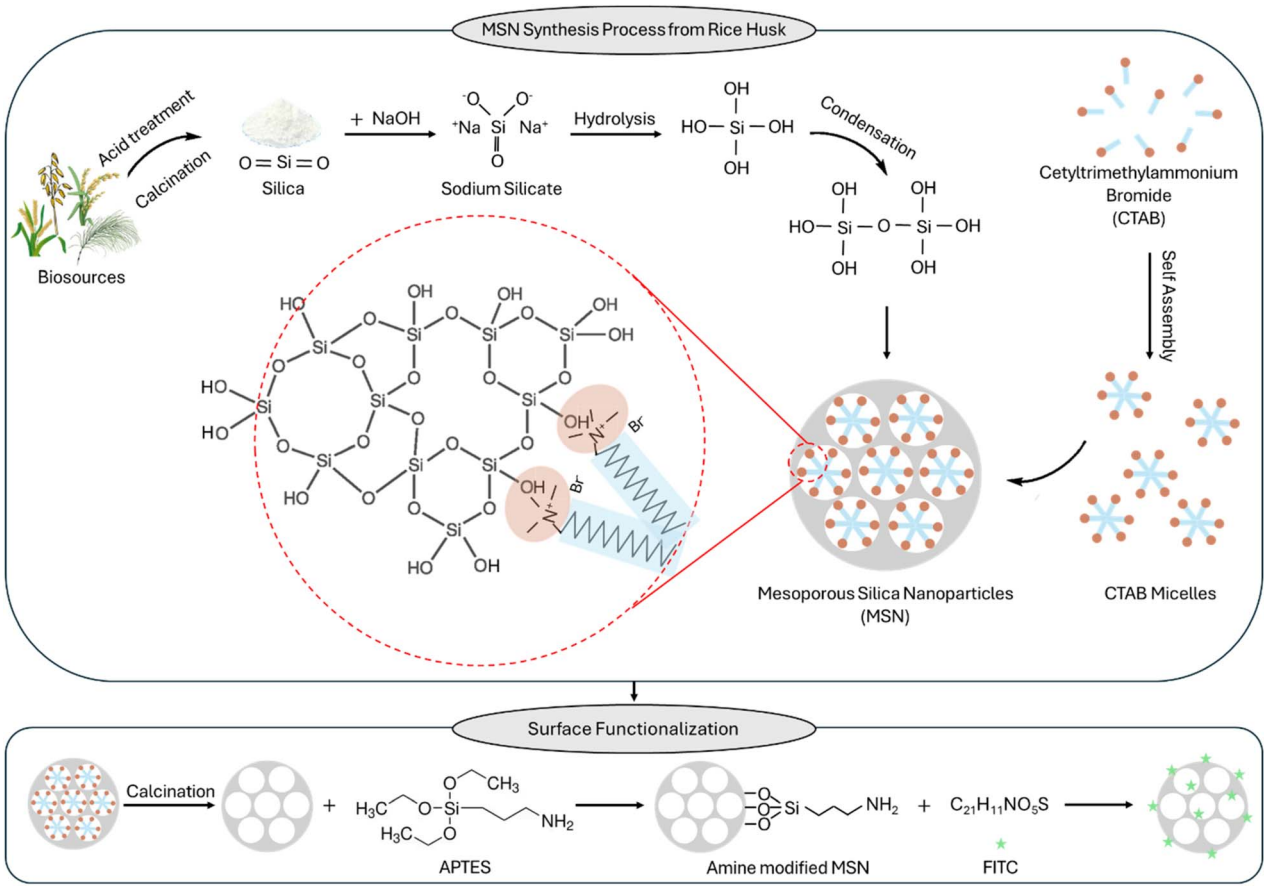

Scheme 1 Schematic overview of the experimental workflow, including silica extraction from biowaste precursors, MSN synthesis and surface functionalization.

was modified with amine groups using APTES. To do this, 100 mg of RMSN was refluxed in 30 mL ethanol containing 1 mL APTES for 6 h at 120 °C.[34] The amine-modified RMSN was collected *via* centrifugation at 6000 rpm for 20 min, washed twice with ethanol, and then dried at 50 °C overnight.[34] Next, APTES functionalized RMSN was dispersed in 50 mL of ethanol containing 5 mg of FITC.[35] The reaction was carried out at room temperature for 24 h under constant stirring at 550 rpm.[35] The FITC labeled RMSN (FITC-RMSN) was then centrifuged, washed three times with ethanol and deionized water to remove unbound FITC. The remaining ethanol was allowed to evaporate, and finally, the dried FITC-RMSN was stored at 8 °C for further use.

Characterization of samples

FT-IR spectra of biowaste-derived ashes and MSNs were obtained using an FT-IR spectrophotometer (TENSOR 27, Bruker, Germany). X-ray diffraction (XRD) patterns were recorded using a powder X-ray diffractometer (D8 Advance, Bruker AXS, Germany) over a 2θ range of 10–90°. The specific surface area and pore size distribution was analyzed using a Belsorp mini (Japan) based on Brunauer–Emmett–Teller (BET) method. The Barrett–Joyner–Halenda (BJH) method was employed to determine the pore size distribution of RHA, HTA, RMSN, and HMSN. Thermogravimetric analysis (TGA) was performed using an SII TGA 6300 (USA) with a heating rate of 10 °C min^{-1} heating rate under air atmosphere. Morphological analysis was conducted using field emission scanning electron microscopy (FE-SEM, TESCAN Vega 3, Czech Republic) and high-resolution transmission electron microscopy (HR-TEM, JEOL JEM-ARM200CFEG UHR-TEM, Japan). Flow cytometry (Cytoflex, Beckman Coulter, USA) was used to quantify cell uptake of FITC-labeled nanoparticles on HUVEC. Cell viability was measured using an MTT assays and the outcome of the plate was read on a Tecan Infinite m200 pro microplate reader (TECAN, Switzerland). Fluorescence microscopy (Axio Observer Z1, Zeiss, Germany) was used to visualize FITC-labeled RMSN in 488 nm and ZO-1 tight junction proteins at 555 nm in HUVECs.

Drug loading and release studies

For drug loading, 5 mg of RMSN or HMSN was dispersed in 5 mL of distilled water, followed by the addition of 5 mg of Dox. The dispersion was stirred at room temperature for 24 h.[6,7,33,35] The mixture was centrifuged at 10 000 rpm for 20 min, and the supernatant was analyzed using a UV spectrophotometer at 482 nm to quantify unloaded drug. The experiment was performed in three replicas. The encapsulation efficiency (EE%) and drug loading capacity (DL%) were calculated as follows:

$$\text{EE (\%)} = (\text{Initial Dox} - \text{Unloaded Dox})/(\text{Initial Dox})$$

$$\text{DL (\%)} = (\text{Initial Dox} - \text{Unloaded Dox})/(\text{MSN weight})$$

For *in vitro* drug release, drug-loaded nanoparticles were dispersed in PBS (5 mL) at pH 7.4 and 5.6,[6,7,33] and then transferred into a shaker incubator to be incubated at 37 °C for 120 h. At predetermined time points, the nanoparticles were centrifuged, and the supernatant was replaced with fresh PBS. The amount of released drug was quantified using a UV spectrophotometer with a detection wavelength of 482 nm.[6,7,33,35] All release studies were performed in triplicate.

Cell culture and cytotoxicity assays. Human umbilical vein endothelial cells (HUVEC), human dermal fibroblast (HDF), and human glioblastoma (U87) cells were gifted by scientist at Ege University, Koc University, and Hacettepe University, respectively, cultured in high glucose DMEM (Gibco) supplemented with 10% (v/v) FBS and 1% (v/v) penicillin-streptomycin at 37 °C in 5% CO_2 atmosphere. Cytotoxicity of MSNs was assessed *via* MTT assay. Briefly, cells (5×10^3 cells per well) were seeded in 96-well plates and allowed for attachment in an incubator with 5% CO_2 at 37 °C for overnight. To analyze safety and biocompatibility of nanoparticles, HUVEC, HDF, and U87 cells were treated with MSNs (1–400 μg mL^{-1}) for 24 h, 48 h, and 72 h. In the aim of toxicity investigation of Dox loaded nanoparticles, U87 cells were treated with Dox loaded-nanoparticles at Dox concentration ranges of 0.08 to 50 μg mL^{-1} for 24 h, 48 h, and 72 h. After each treatment, 20 μL of MTT reagent (5 mg mL^{-1} in PBS) was added to each well for 3 h, formazan crystals were dissolved in DMSO (100 μL). Absorbance at 570 nm was recorded. All experiments were conducted in three replicates.

Cell binding assay by flow cytometry

To evaluate the binding ability of FITC-RMSNs to HUVEC and U87 cells, a cell binding assay was performed. Briefly, 2×10^5 viable cells were seeded into 12-well plates and incubated at 37 °C for 24 h. Prior to treatment, the plates were placed on ice for 15 min. Cells were then treated with FITC-RMSNs at varying concentrations (1, 4, 10, 25, 50, 100, and 200 μg mL^{-1}) and incubated on ice for 2 h. Following treatment, the cells were washed three times with DPBS, scraped from the wells, resuspended in DPBS, and fixed in 70% cold ethanol. After redispersion in DPBS, the samples were analyzed by flow cytometer. All experiments were conducted in triplicate.

Cell uptake assay by flow cytometry

A 2D cell uptake assay was performed to assess the internalization of FITC-RMSNs by HUVEC and U87 cells. Briefly, 2×10^5 viable cells were seeded into 12-well plates and incubated at 37 °C for 24 h. Subsequently, FITC-RMSNs were introduced at concentrations of 1, 4, 10, 25, 50, 100, and 200 μg mL^{-1}, and cells were incubated for 4 h. Post-incubation, cells were washed three times with DPBS, trypsinized, and fixed with 70% cold ethanol before analysis by flow cytometer. All experiments were performed in three replicates.

Cell uptake assay by fluorescent microscopy

HUVEC and U87 cells were seeded into 12-well plates at a density of 1×10^5 cells per well and incubated for 24 h. The culture medium was then replaced with refresh medium containing red-dye cell tracker (1 : 100 dilution), and incubation continued for another 24 h. Following this, FITC-RMSNs at concentrations of 50, 200, and 400 μg mL^{-1} were introduced and incubated for 4 h. Cells were subsequently washed multiple times with DPBS and visualized using fluorescence microscopy.

Chip fabrication

A single-channel structure in a microfluidic chip was fabricated to mimic the 3D structure of the human vasculature. The chip was produced using a casting method, where a PDMS/curing agent mixture (10 : 1 ratio) was blended, and poured into 3D-printed molds, degassed under vacuum to remove bubbles, and cured at 60 °C for 6 h. The resulting microchannels has dimensions of 300 μm (width), 300 μm (thickness), and 2 cm (length). The PDMS chips were then removed from the molds, cleaned with isopropanol, followed by distilled water, and dried using nitrogen gas. To bond the top and bottom layers, oxygen plasma treatment was applied using Diener Zepto plasma cleaner (USA). Before cell culturing, chips were inspected for delamination, debris, or other defects.

Cell culture in microchannels

Microchannels underwent surface coating for optimal cell adhesion. First, channels were coated with APTES for 20 min at room temperature, followed by three washes with DPBS. Chips were then exposed to UV light (365 nm) for 15 min. A collagen-fibronectin mixture (100 μg mL^{-1} 1 : 1) was applied, and chips were incubated overnight. After washing with DPBS twice, HUVEC and U87 cells were injected at density of 2×10^4 cell per μL in different chips and incubated for 24 h. The culture medium was then refreshed, and the chips were maintained in an incubator for further analysis.

Cell uptake study in microfluidic chips

Microfluidic chips were treated with FITC-RMSNs under two conditions: (i) static incubation and (ii) dynamic incubation under flow. In static conditions, straight and serpentine channels were treated by 20 μL of FITC-RMSNs (100 μg mL^{-1}) and incubated for 4 h. For dynamic conditions, channels were connected to a peristaltic pump *via* sterile tubing and continuously treated with FITC-RMSNs (100 μg mL^{-1}) at a flow rate of 60 μL h^{-1} at 37 °C for 4 h. Following incubation, microchannels were washed three times with DPBS to remove unbound RMSNs before immunostaining. Finally, immunostaining was performed to observe cellular uptake of FITC-labeled RMSN.

Immunostaining assays

Immunostaining was performed on HUVEC cells which contain ZO-1 protein to identify cells boundary. Microchannels were washed three times with DPBS+/+ to remove excess RMSNs. Cells were fixed with ice-cold methanol for 20 min at room

temperature in the dark. After methanol removal, cells were rewashed with DPBS +/+ 3 times. Protein blocking was performed using by 1.5% BSA in DPBS+/+ for 1 h at room temperature. Cells were then incubated overnight at 4 °C in the dark with primary rabbit anti-human anti-ZO1 (zonula occludens-1) polyclonal antibody (ProteinTech, 21773-1-AP, 1 : 1000 dilution) in blocking buffer. Following three 5-minute washes with DPBS+/+, seconday Cy3 AffiniPure Goat Anti-Rabbit IgG (H + L) (Jackson ImmunoResearch, 111-165-003, 1 : 500 dilution in blocking buffer) was applied for 1 h at room temperature in the dark. After another three 5-minute washes with DPBS+/+, DAPI (1 : 1000 in DPBS+/+) was incubated for 2 min at room temperature in the dark. A final wash step with DPBS+/+ was performed three times for 5 min. Imaging was conducted using Axio Observer Z1 ZEISS fluorescence microscopy.

Results

Characterization of biowastes

Various bio-sources and biowastes naturally contain silica in their structure,[24,26] therefore they can be an ideal source for sustainable, cost-effective, and abundant sources for generating silica-based products. In this study, we aimed to identify the most efficient biowaste sources for silica isolation, with the ultimate goal of utilizing them in drug delivery applications. For silica isolation, six biowastes (RH, HT, WH, WS, OH, OS) were selected. Silica was extracted using acid treatment followed by calcination. The resulting silica samples (RHA, HTA, WHA, WSA, OHA, and OSA) were characterized using FTIR and XRD. Additionally, the conversion efficiency of biowaste to silica was assessed through TGA.

Fig. 1A and B demonstrates the FTIR and XRD analyses of the extracted silica. The FTIR spectra of all samples exhibited similar patterns, consistent with that of pure silica.[36] Characteristic silica absorption bands located at 436 cm^{-1} (Si–O–Si bending vibration), 795 cm^{-1} (Si–O–Si symmetric stretching), and 1036 cm^{-1} (Si–O–Si asymmetric vibration).[37] Additionally, a peak at 3350 cm^{-1} corresponded to the symmetric stretching of the Si–OH group, while an adsorption band at 1620 cm^{-1} was attributed to O–H stretching from adsorbed water.[5] These findings confirm the successful extraction of silica from biowastes without significant impurities. The XRD patterns of the biosilica extracted from various biowaste sources and the synthesized MSNs are shown in Fig. X. All biosilica samples exhibited a broad diffraction peak around $2\theta \approx 22°$, which corresponds to the amorphous structure of silica, consistent with standard reference data (JCPDS card no. 29-0085).[38,39] The absence of additional crystalline peaks further confirmed that the high purity of the extracted silica.

While FTIR and XRD analysis validated the purity of the isolated silica, the efficiency of extraction is a crucial factor in selecting the optimal biowaste source. TGA (Fig. 1C) was conducted to evaluate the decomposition behavior of the raw biowastes. TGA curves for all biowaste sources revealed three distinct weight loss stages: (1) 100–190 °C related to related to moisture release and light volatiles, (2) 200–310 °C related to decomposition of organic components including cellulose, hemicellulose and lignin, and (3) 360–800 °C related to formation and release of CO and CO_2 gases. Following complete combustion, the residual ash primarily consisted of silica. TGA data indicated that the ash content of the biowastes was as follows: 25.92% of RH, 26.84% of HT, 15.58% of WH, 12.17% of WS, 13.8% of OH, and 8.47% of OS. To quantify silica yield, the conversion efficiency of dried biowastes to silica was calculated (Fig. 1D). The results showed that the content was 22.20% for RH, 9.30% for HT, 2.10% for WH, 2.22% for WS, 2.92% for OH, and 2.43% for OS. Comparison with the TGA-derived ash content revealed that 85% of RH ash and 34.64% of HT ash consisted of silica, whereas the other biowastes contained negligible amounts. These values are consistent with previous reports in the literature, which highlight RH and HT as a particularly silica-rich biowaste materials.[40,41]

Based on these findings, RH and HT were identified as the most efficient sources for silica extraction, making them the preferred biowastes subsequent synthesis of MSNs; therefore, these two biowaste were used in the following experiments.

Characterization of MSNs

The aim of synthesizing MSNs is to develop nanoscale carriers with an increased specific surface area, enabling further surface modifications and functionalization for enhanced applications in targeted nanomedicine and drug delivery. The pore diameter and average pore volume are critical parameters that influence the drug delivery potential of these nanocarriers and can be optimized by selecting an appropriate surfactant. In this study, RH and HT were identified as the most suitable precursors for conversion into MSNs. Using CTAB as a surfactant, RMSN and HMSN were synthesized *via* the sol–gel method.[6,7] To analyze the chemical composition of the synthesized RMSN and HMSN, FTIR spectroscopy and XRD were employed. Fig. 2A presents the FTIR spectra of RMSN and HMSN, where characteristic silica network peaks are observed at 436, 795, and 1036 cm^{-1}. A prominent peak at 957 cm^{-1}, attributed to the silanol (–Si–OH) group, indicates potential for further surface modification. Fig. 2B displays the XRD patterns of RMSN and HMSN over a 2θ range of 10 to 90°. A broad peak at 22° corresponds to silica network[6] confirming the successful synthesis of silica. The absence of additional peaks in both FTIR and XRD analyses suggests the high purity of the synthesized MSNs.

To assess mesoporosity of RMSN and HMSN, BET/BJH surface analysis was conducted for RHA, HTA, RMSN and HMSN. Fig. 2C illustrates the N_2 adsorption/desorption isotherms of these samples. According to IUPAC classification, the RMSN and HMSN isotherms exhibit a type IV profile,[42] indicative of mesoporous structure, where adsorption reaches saturation in subsequent layers. A more detailed examination reveals that the RMSN follows a type IV(a) isotherm with a pore condensation and H1-type hysteresis, signifying the presence of cylindrical pores with uniform diameters and open ends.[43] Conversely, HMSN follows a type IV(b) isotherm, representing mesoporous materials with cylindrical pores less than ~4 nm for nitrogen at 77 K.[44] H4 type hysteresis observed in RHA and

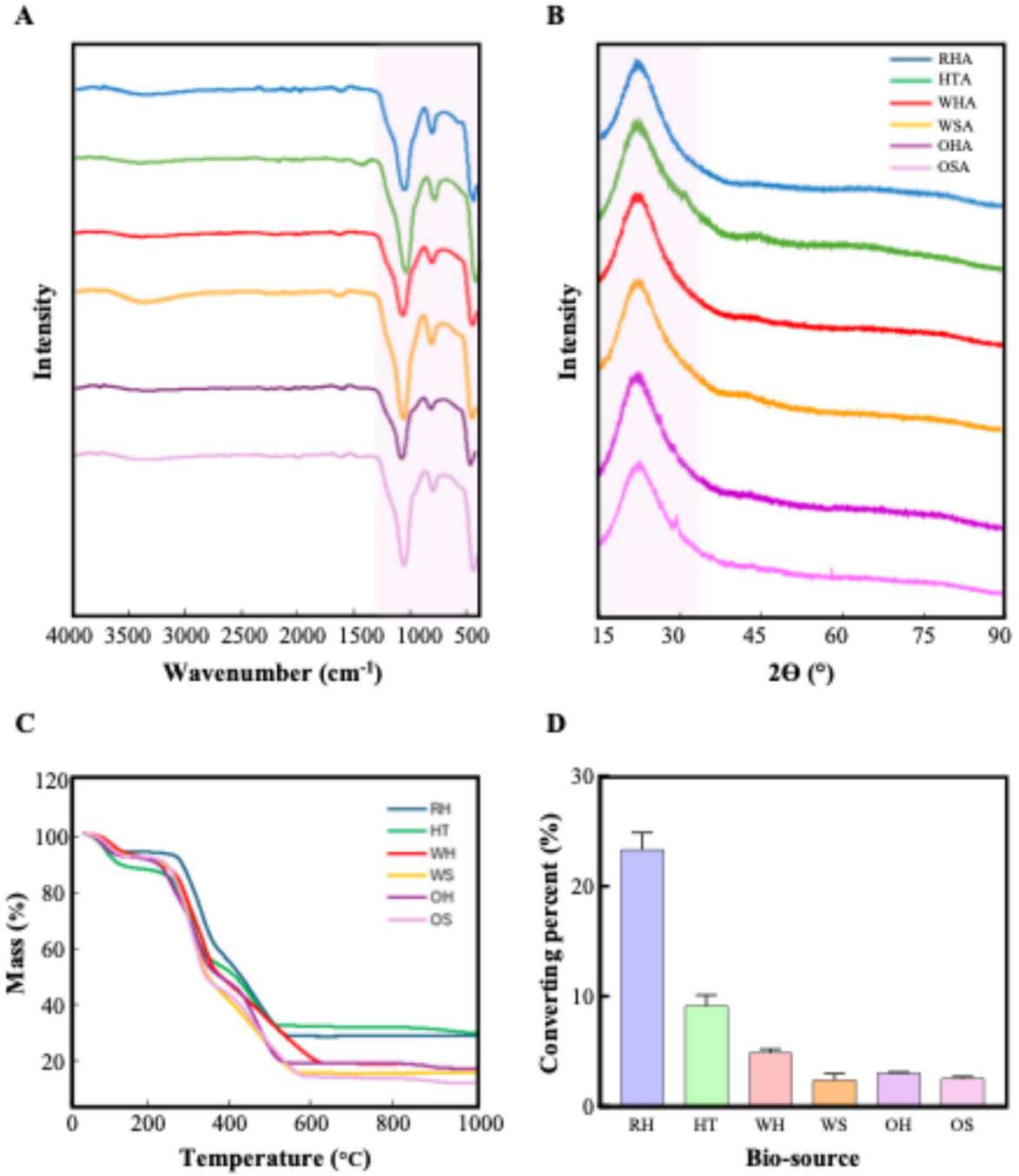

Fig. 1 Physicochemical characterization of biowastes and their ashes. (A) FT-IR, (B) normal XRD patterns of RHA (blue), HTA (green), WHA (red), WSA (yellow), OSA (purple), OSA (pink), (C) TGA analysis, and (D) converting percent of RH (blue), HT (green), WH (red), WS (yellow), OS (purple), OS (pink).

HTA suggests the presence of slit-shaped pores, typically found in mixed microporous and mesoporous materials.[45] These findings indicate that the sol–gel process effectively transform the pore structure of RMSN and HMSN into cylindrical form, which is highly advantageous for drug delivery and nanomedicine applications.[46] BET analysis revealed that the specific surface areas of RHA and HTA were 343 cm^2 g^{-1} and 254 cm^2 g^{-1}, respectively, with average pore volumes of 0.37 cm^3 g^{-1} and 0.43 cm^3 g^{-1}. Through the sol–gel process by surfactant addition, the specific surface area significantly increased after MSNs synthesis. The specific surface areas of RMSN and HMSN were measured at 1538 cm^2 g^{-1} and 1357 cm^2 g^{-1}, respectively, with corresponding average pore volumes of 1.4, and 0.9 cm^3 g^{-1}, demonstrating a substantial improvement in surface characteristics.

Fig. 2D depicts the pore size distribution of RHA, HTA, RMSN, and HMSN. RHA and HTA exhibit board pore size distribution, with average pore diameter of 4.16 and 6.7 nm,

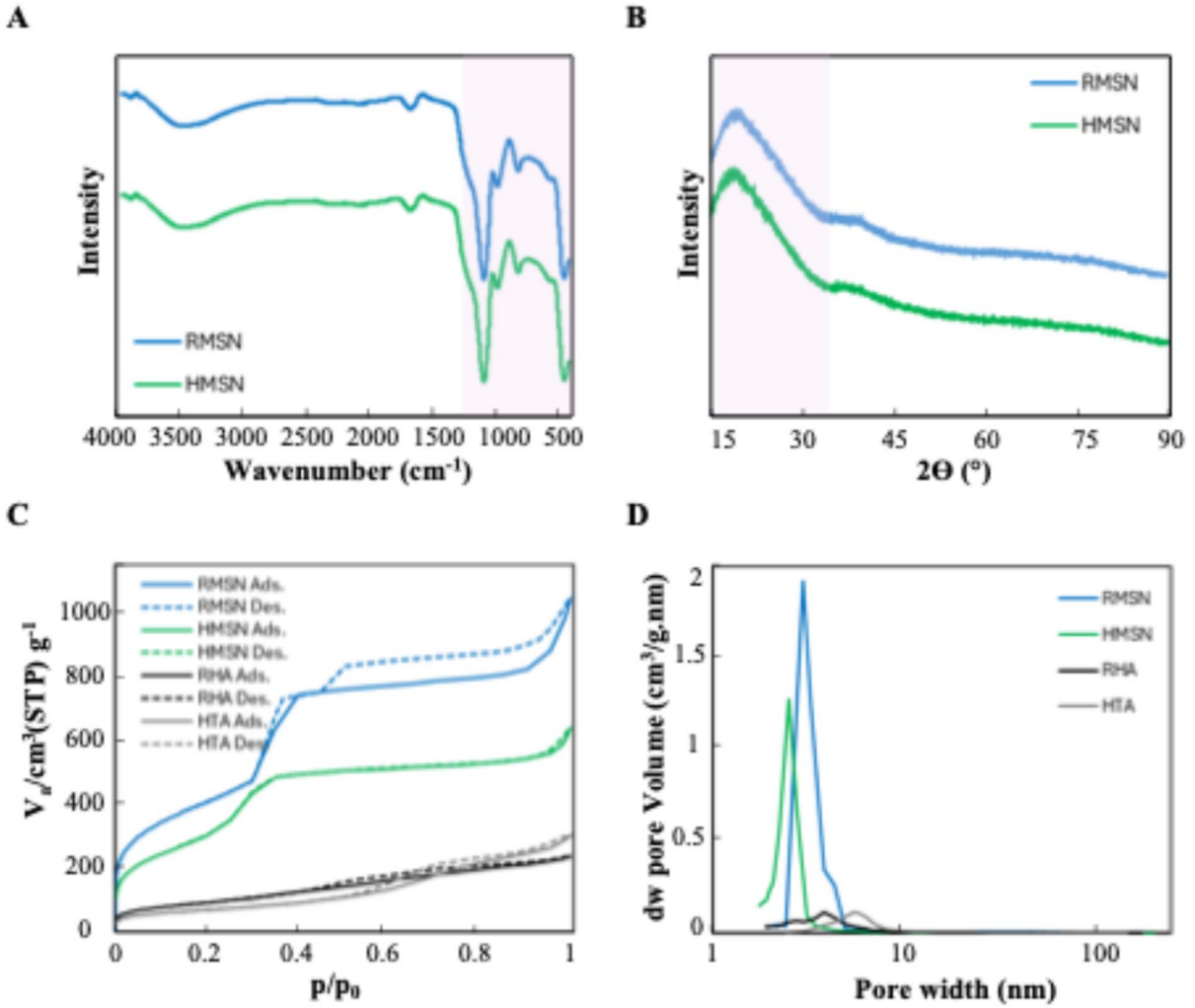

Fig. 2 Physicochemical characterization of mesoporous silica nanoparticles (MSNs). (A) FT-IR, (B) normal XRD patterns of RMSN (blue), HMSN (green) (C) BET surface analysis, and (D) BJH analysis of RMSN (blue), HMSN (green), RHA (black), HTA (grey).

respectively. Following the conversion to RMSN and HMSN, a smaller pore size distribution is observed, with average pore diameters of 3.7 and 3.1 nm, respectively. These results confirm the successful formation of mesoporous silica structures with controlled pore size reduction.

HR-TEM was employed to further investigate the mesoporosity of the nanoparticles. Fig. 3A and B display HR-TEM images of bulk RMSN and HMSN powders, respectively. Structural analysis reveals that RMSNs exhibit a regular hexagonal morphology with a smaller particle size than HMSNs. The synthesis of RMSNs from RH biowaste results in distinct nanoparticle boundaries and uniform morphology. The average hydrodynamic diameters of RMSN and HMSN were measured at 30 ± 2 and 48 ± 3.6 nm, respectively. Given that both nanoparticles synthesized using the same method, the observed size differences can be attributed to variations in the precursor materials. HR-TEM imaging, widely recognized as an effective technique for studying porous materials, further confirms the highly ordered mesoporous structures of RMSN and HMSN, aligning with the BET/BJH results (Fig. 2C and D).

Dox loading and release studies

To assess the drug delivery potential of the synthesized RMSN and HMSN, Dox, a model anticancer drug, was loaded into the nanoparticles.

To evaluate the drug release behavior of RMSNs and HMSNs, pH 7.4 and pH 5.6 have been selected as representative physiological and pathological conditions, respectively. The pH 7.4 simulates the normal physiological pH of blood and healthy tissues,[47] while pH 5.6 reflects the mildly acidic microenvironment commonly found in tumor tissues and intracellular compartments such as endosomes and lysosomes.[48,49] Dox cumulative release behavior was evaluated at pH levels of 7.4 and 5.6 over a period of 120 h. Surface properties such as specific surface area, pore size and pore shape are critical parameters influencing the drug delivery efficiency of nanocarriers.[6,50] The LE of RMSN and HMSN was determined to be 70 ± 1.05 and 68 ± 3.9%, respectively. Additionally, their EE% was 53 ± 1.2 and 54 ± 1.9%, indicating a high efficiency of drug loading and encapsulation by both RMSN and HMSN. The

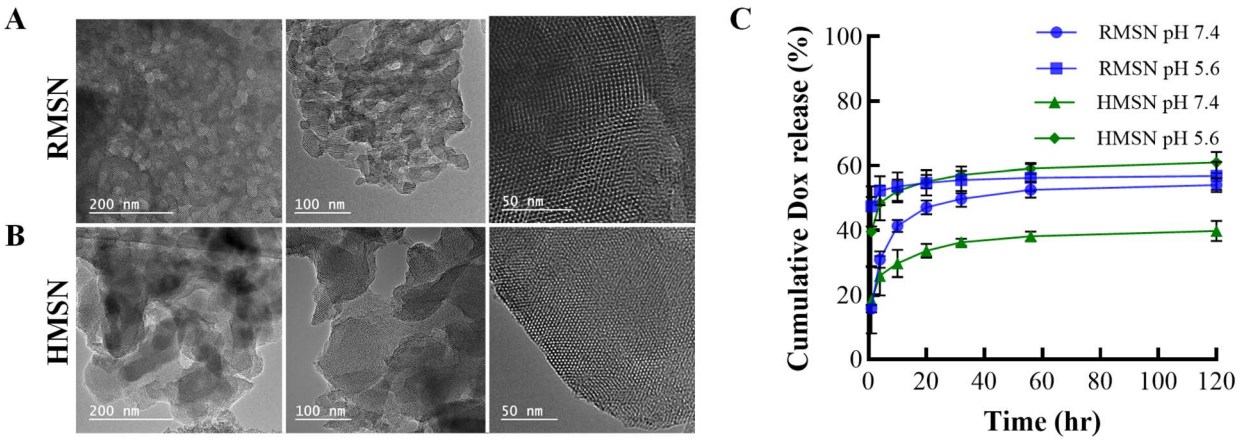

Fig. 3 HR-TEM images of (A) RMSN and (B) HMSN. (C) The *in vitro* doxorubicin (Dox) release of Dox loaded RMSN (blue) and Dox loaded HMSN (green) at different pH values (pH = 7.4 and 5.6).

cumulative release profiles of Dox from RMSN and HMSN were examined at two different pH levels, simulating the acidic tumor microenvironment and the physiological pH of healthy tissues. The results were reported in Fig. 3C. In both RMSN and HMSN release profiles, the cumulative release of Dox was higher at pH 5.6 compared to pH 7.4. This behavior is attributed to the pH-dependent solubility of Dox,[51] as the protonation of amine groups enhances its solubility under acidic conditions. Conversely, solubility decreases as the pH shifts from 5.6 to 7.4.[6,7,33,51] This pH-dependent release is more pronounced in the initial phase. Within the first hour, approximately 15% of Dox was released from RMSN at pH 7.4, whereas 53% was released in acidic conditions. For HMSN, the corresponding release percentages were 30% and 51%. After 4 h, these values increased to 31% and 55% for RMSN and 33% and 55% for HMSN, respectively. These findings suggest that RMSN exhibits a higher pH sensitivity in the early stages of drug release. After 4 h, the drug release of Dox from RMSN at pH 7.4 continued to increase over time, while no significant additional release was observed at pH 5.6. In contrast, HMSN showed a steady increase in drug release at both pH levels. As a result, the difference in cumulative Dox release between pH 7.4 and 5.6 was more pronounced for HMSN than for RMSN. Overall, these findings confirm that both RMSN and HMSN are capable of drug loading and controlled release, making them promising candidates for drug delivery applications.

Cytotoxicity characterization of RMSN and HMSN

The biocompatibility of RMSN and HMSN was assessed by treating HDF, HUVEC, and U87 cells with blank nanoparticles with concentration ranging from 1 to 400 μg mL^{-1} for 24, 48, and 72 h. The cell viability percentages of HUVEC, HDF, and U87 cells following incubation with RMSN and HMSN are presented in Fig. 5A. The results indicate that RMSN and HMSN exhibit no significant toxicity toward HDF, HUVEC cells. To further validate this finding, the same treatment was applied to U87 cells, another human-derived healthy cell line, which yielded consistent results. These findings demonstrate the strong biocompatibility of nanocarriers. Consequently, these biogenic drug delivery systems, with their excellent biocompatibility, hold great potential as effective drug delivery platforms in cancer therapy. To evaluate the drug delivery potential of the nanoparticles in cancer cells, Dox loaded RMSNs and HMSNs were incubated with U87 cells for 24, 48, and 72 hours. The resulting cytotoxicity data are presented in Fig. 4B. The results clearly demonstrate that increasing Dox concentration leads to a significant reduction in U87 cell viability, even at relatively low doses. Furthermore, prolonged incubation times amplified the cytotoxic effect at each concentration. Notably, Dox loaded RMSNs exhibited a stronger cytotoxic effect compared to Dox loaded HMSNs, which is consistent with the drug release profiles. RMSNs released a greater amount of Doxorubicin over the same period compared to HMSNs. These findings indicate that RMSNs possess a higher drug delivery efficiency and therapeutic potential against cancer cells.

Among all the tested biowaste precursors, RH and HT exhibited the highest silica yield and purity, making them the most promising candidates for MSN synthesis. Upon further comparison of the MSNs synthesized from these two sources, RMSNs demonstrated superior textural properties, including a higher surface area and more uniform mesopore structure, as confirmed by BET and TEM analyses. Additionally, RMSNs showed enhanced drug loading capacity and more favorable release kinetics in acidic conditions, which are desirable for tumor-targeted delivery. Moreover, Dox-loaded RMSNs showed a greater therapeutic effect against U87 cancer cells. Based on these findings, RMSNs were selected as the optimal nanocarrier for subsequent biological evaluations. This selection ensures consistency and maximizes the therapeutic potential of green-synthesized MSNs.

2D cellular uptake visualizing by a fluorescent microscopy

To investigate cellular internalization of the nanoparticles, RMSN was first modified with APTES for covalent conjugation with FITC. The FITC-labelled nanoparticles were then incubated with HUVEC and U87 cells for 4 h at the concentration of

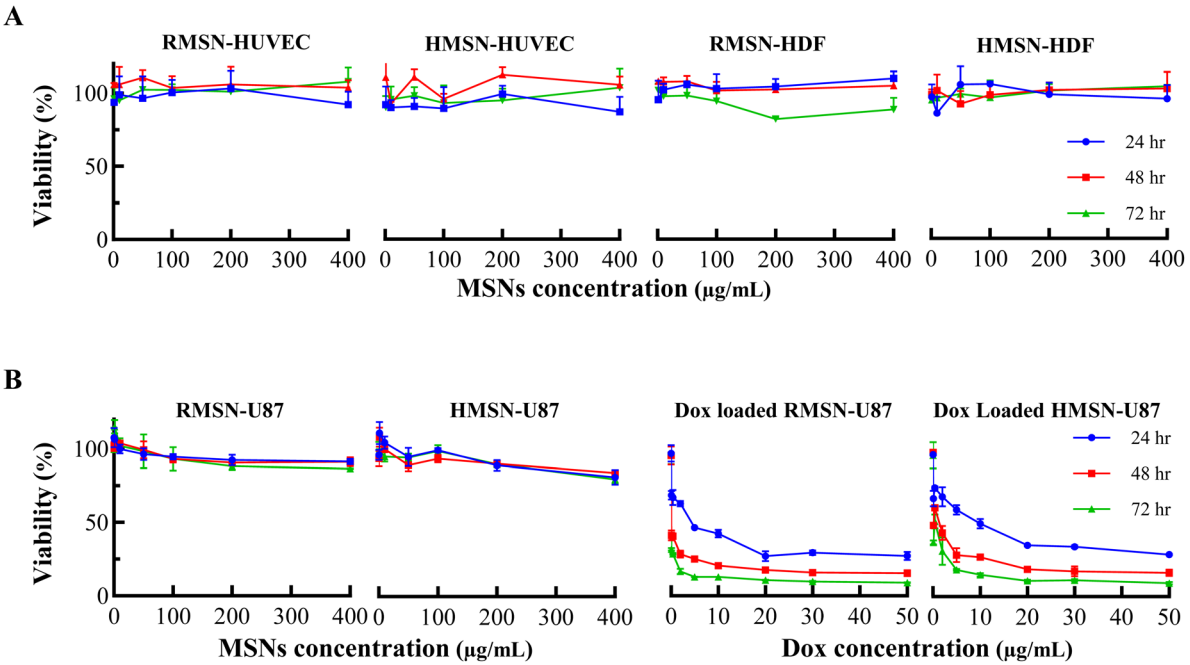

Fig. 4 Biocompatibility and biosafety evaluation of MSNs on HUVEC, HDF, and U87 cells, as well as the cytotoxicity analysis of Dox-loaded RMSN and HMSN on U87 cells using the MTT assay. (A) Cell viability of HUVEC and HDF cells treated with blank RMSN and HMSN at nanoparticle concentrations ranging from 1 to 400 μg mL^{-1} for 24, 48, and 72 hours. (B) Cell viability of U87 cells treated with blank RMSN and HMSN at the same concentration range, and with Dox-loaded RMSN and HMSN at Dox concentrations ranging from 0.08 to 50 μg mL^{-1} for 24, 48, and 72 hours (the statistical analysis between Dox loaded nanoparticles compared with unloaded nanoparticles involved in the SI data. All comparisons showed *P*-value < 0.0001).

50, 200, 400 μg mL^{-1}. The cytoplasm of HUVECs and U87s was pre-stained with a red cell tracker dye to visualize cellular localization. Fig. 5 illustrates the cellular uptake capability of FITC-RMSN, as observed through fluorescent microscopy. The results confirm that FITC-RMSNs were successfully internalized and predominantly localized in the cytoplasm of cells. The extent of cellular uptake exhibited a strong dependence on FITC-RMSN concentration. The extent of cellular uptake exhibited a strong dependence on FITC-RMSN concentration. At a concentration of 50 μg mL^{-1}, higher fluorescence intensity was observed in U87 cells compared to HUVECs. However, as the concentration increased, this trend reversed, and greater FITC intensity was detected in HUVECs. This observation may be explained by several factors. First, HUVECs are morphologically larger than U87 cells (approximately two-fold) and possess a greater membrane surface area, which may facilitate increased nanoparticle contact and internalization.[52,53] Second, the reversal may be due to a saturation effect in U87 cells, where endocytic pathways reach a threshold beyond which additional nanoparticles are not effectively internalized. Cancer cells like U87 may also downregulate uptake mechanisms at higher nanoparticle doses to avoid toxicity, leading to self-limiting internalization.[54] Third, the lack of targeting ligands on the MSN surfaces may result in non-specific uptake mechanisms, such as clathrin-mediated or macropinocytosis-based endocytosis, which are active in both cell types.[55,56]

At 400 μg mL^{-1}, although the total amount of internalized FITC-RMSNs increased, no particles were observed within the cell nucleus. Additionally, agglomerated particles were unable to enter the cells due to their larger size. Taken together, these results underscore the complexity of nanoparticle–cell interactions and suggest that, in the absence of targeted modifications, RMSNs are internalized *via* general endocytic pathways with comparable efficiencies in both endothelial and cancer cells. These findings highlight the importance of further surface engineering to enable selective delivery in future applications.

Cell binding and uptake study by flow cytometry

To further investigate the cell binding and uptake of FITC-labeled RMSNs in HUVEC and U87 cells, flow cytometry was employed to quantify the amount of surface-bound and internalized nanoparticles by measuring the mean fluorescence intensity. Fig. 6A presents the binding and uptake fluorescence intensities of HUVEC and U87 cells treated with increasing concentrations of FITC-RMSNs ranging from 1 to 200 μg m^{-1}. Binding experiments were performed on ice to reduce cellular metabolism and inhibit internalization, ensuring that only surface-bound nanoparticles were measured. Additionally, cells were detached using mechanical scraping rather than trypsinization to preserve nanoparticle attachment on the cell surface. At a FITC-RMSN concentration of 1 μg mL^{-1}, 20.61% of HUVEC cells and 20.46% of U87 cells exhibited FITC fluorescence, indicating successful nanoparticle binding. This percentage increased to 55% in HUVEC and 61.83% in U87 cells when the concentration was raised to 25 μg mL^{-1}, demonstrating a dose-dependent binding profile. To evaluate

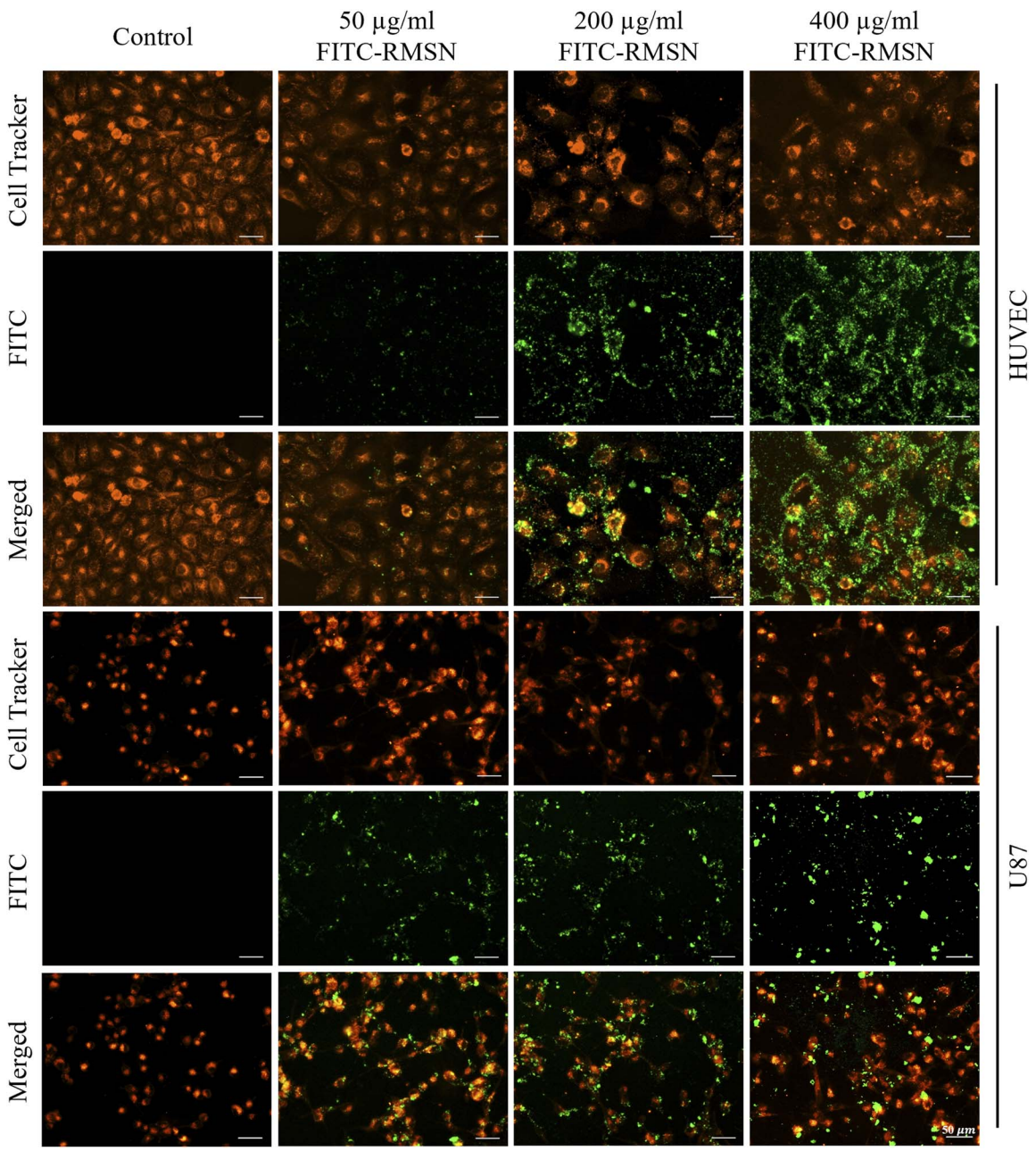

Fig. 5 2D cellular uptake visualization by fluorescent microscopy. Fluorescence microscopy images of HUVEC and U87 cells treated with various concentrations of FITC-RMSN (50, 200, 400 μg mL^{-1}) for 4 h. Cells were pre-stained with a red cell tracker dye to visualize cell localization. The control represents the unlabeled cells. All images were taken at 20× magnification, and the scale bar represents 50 μm.

nanoparticle internalization, a cellular uptake assay was conducted by incubating HUVEC and U87 cells with FITC-RMSNs at 37 °C for 4 hours under conventional 2D culture conditions. The results revealed a direct correlation between nanoparticle concentration and cellular uptake, with higher concentrations leading to increased internalization. Notably, treatment with 25 μg mL^{-1} FITC-RMSNs resulted in 79.58% of HUVEC and 84.99% of U87 cells exhibiting fluorescence, highlighting the efficient internalization of the nanoparticles.

Fig. 6B quantifies the relationship between FITC-RMSN concentration and cell binding in both cell lines, showing that the percentage of bound cells increases with higher nanoparticle concentrations, although the increase is more pronounced at lower concentrations. Fig. 6D illustrates the relationship between FITC-RMSN concentration and cellular uptake percentage, revealing that cellular uptake approaches saturation even at moderate nanoparticle concentrations, indicating a highly efficient internalization mechanism.

However, when comparing the uptake percentages between HUVEC and U87 cells at the same concentration, a slightly lower uptake was observed in U87 cells. This trend is consistent with

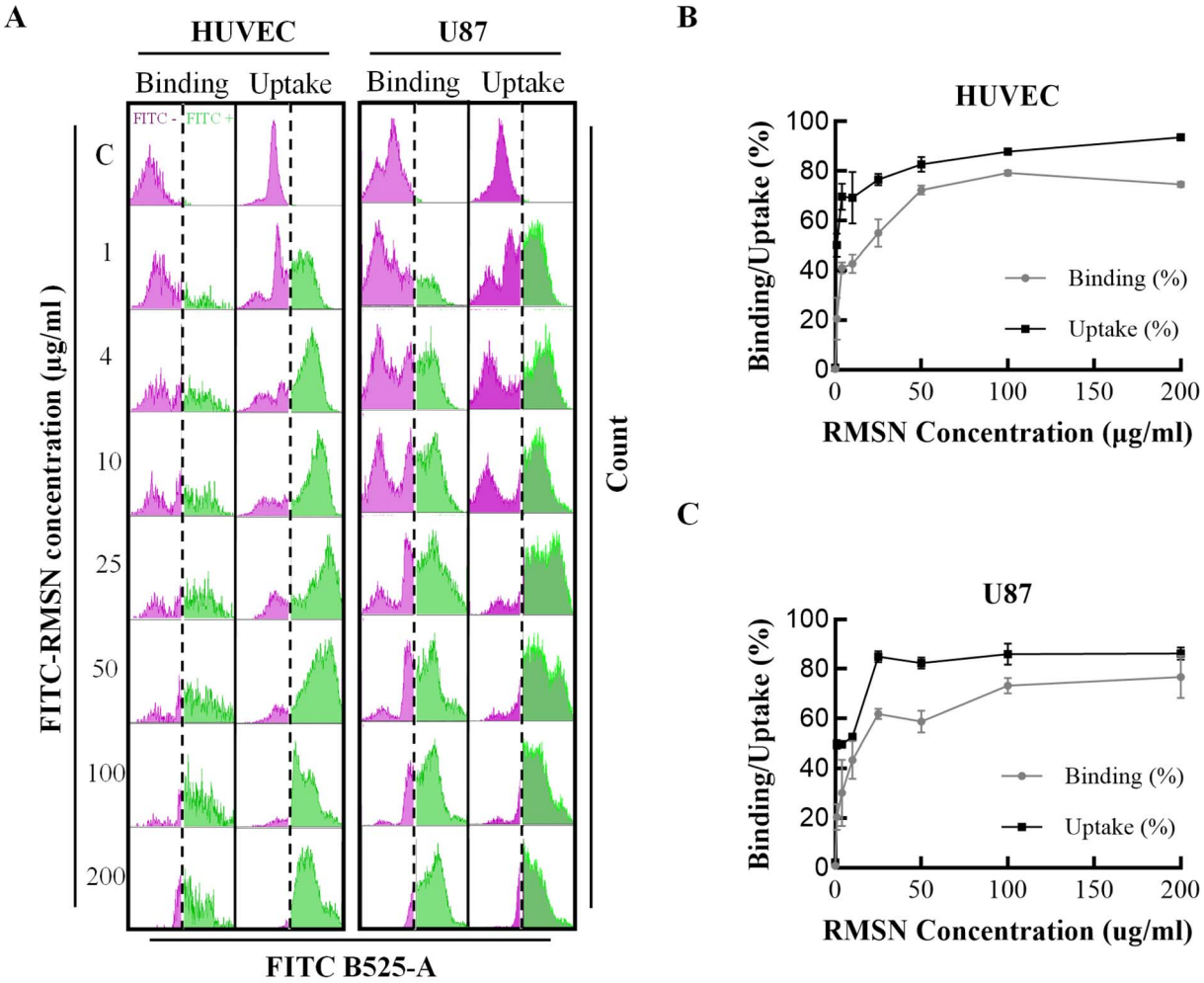

Fig. 6 Cellular binding and uptake analysis of HUVEC and U87 cells treated with different concentrations of FITC-RMSNs. (A) Cellular binding and uptake histograms analysis of FITC-RMSNs at different concentrations (1 to 200 μg mL^{-1}) on HUVECs and U87s performed by flow cytometry, (B) quantification of the cellular binding and uptake activity of FITC-RMSNs on HUVECs at different concentrations, (C) quantification of cellular binding and uptake percentage as a function of FITC-RMSN concentration on U87 cells. Control represents the cells without RMSN treatment.

the fluorescent microscopy observations described in the previous section.

Cellular uptake of MSNs in 3D microfluidic chips

A microfluidic device was utilized to create a 3D environment for culturing HUVECs, and U87, mimicking physiological vascular conditions. This system enabled continuous fluid flow, replicating blood circulation and providing a more physiologically relevant setting compared to traditional static 2D culture models. In the static condition (Fig. 7A), no continuous flow of medium was applied, allowing the nanoparticles to interact with the cells inside the microfluidic channel in a localized manner without the influence of fluid motion, as in the traditional cellular uptake studies. In contrast, the dynamic model (Fig. 7B) applied a continuous media flow at a rate of 60 μL h^{-1}, simulating physiological blood circulation. This setup facilitates the observation of nanoparticle movement and potential effects of shear stress cellular uptake. FITC was used to track the localization of RMSNs, while ZO-1 staining was employed to visualize cell borders and assess whether FITC-RMSNs were internalized or remained extracellular in HUVEC cells. On the other hand, due to the naturally low expression of ZO-1 in U87 cells, Bright Field imaging was used to identify the cell borders in this cell line. The cell nuclei were also stained with DAPI.

Fig. 7C and 8 illustrate the fluorescence microscopy images of stained HUVEC, and U87 cells, respectively. The fluorescence microscopy images captured at 10× or 63× magnifications demonstrate that under static conditions, only a small amount of FITC-RMSN was internalized by the cells. However, under dynamic conditions, 10× images displayed an overall increase in nanoparticle presence on the cells under, while the 63× images revealed that RMSNs were primarily localized within the cytoplasm, with higher fluorescence intensity compared to static conditions. It is also evident that the increase in FITC-RMSN uptake under continuous conditions, compared to stationary conditions, is more pronounced in the U87 cells than in the HUVEC cell line.

Additionally, imaging results indicated morphological differences between cells in the static and dynamic models in

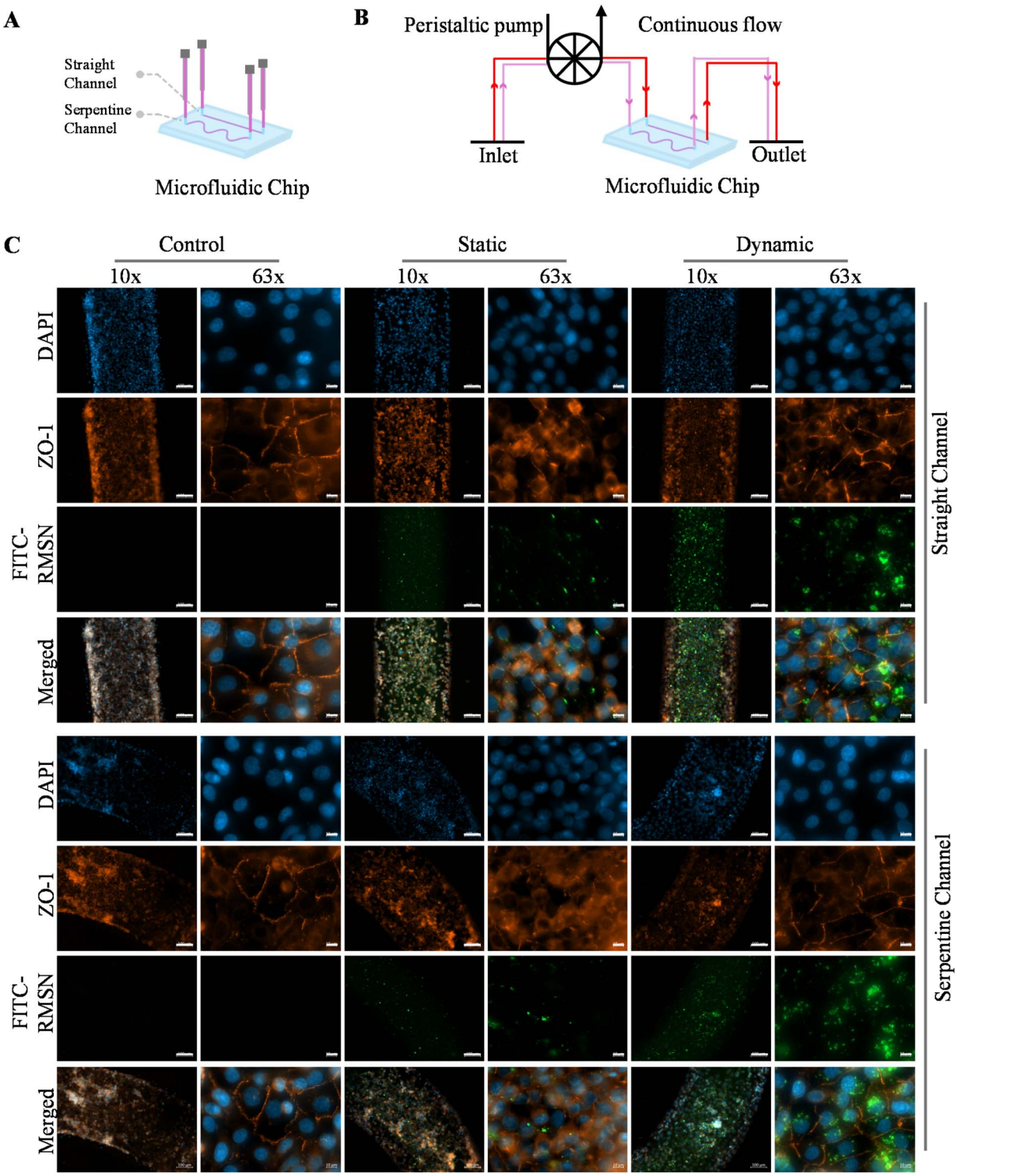

Fig. 7 3D cellular uptake study using fluorescent microscopy. Schematic representations of 3D cellular uptake protocol using microfluidic chips under (A) static and (B) continuous flow conditions. (C) Fluorescent images of HUVEC cells performed uptake assays with 100 μg mL^{-1} FITC-RMSN under static and dynamic flow conditions in straight and serpentine single-channel microfluidic chips. The flow rate in the dynamic mode was 60 μL h^{-1}. Cells nuclei were stained with DAPI, while HUVECs were stained with ZO-1, a tight junction protein expressed on the trans-membrane. Scale bars: 100 μm for the 10× images and 10 μm for the 63× images.

both cell lines. Under static conditions, cells appeared smaller and more aggregated, whereas under continuous flow, they exhibited a more spread-out morphology with clearly defined cell borders and increased cell size. This effect was observed in both the straight and serpentine microfluidic channel models (Fig. 7C and 8). Furthermore, a comparison of FITC-RMSN

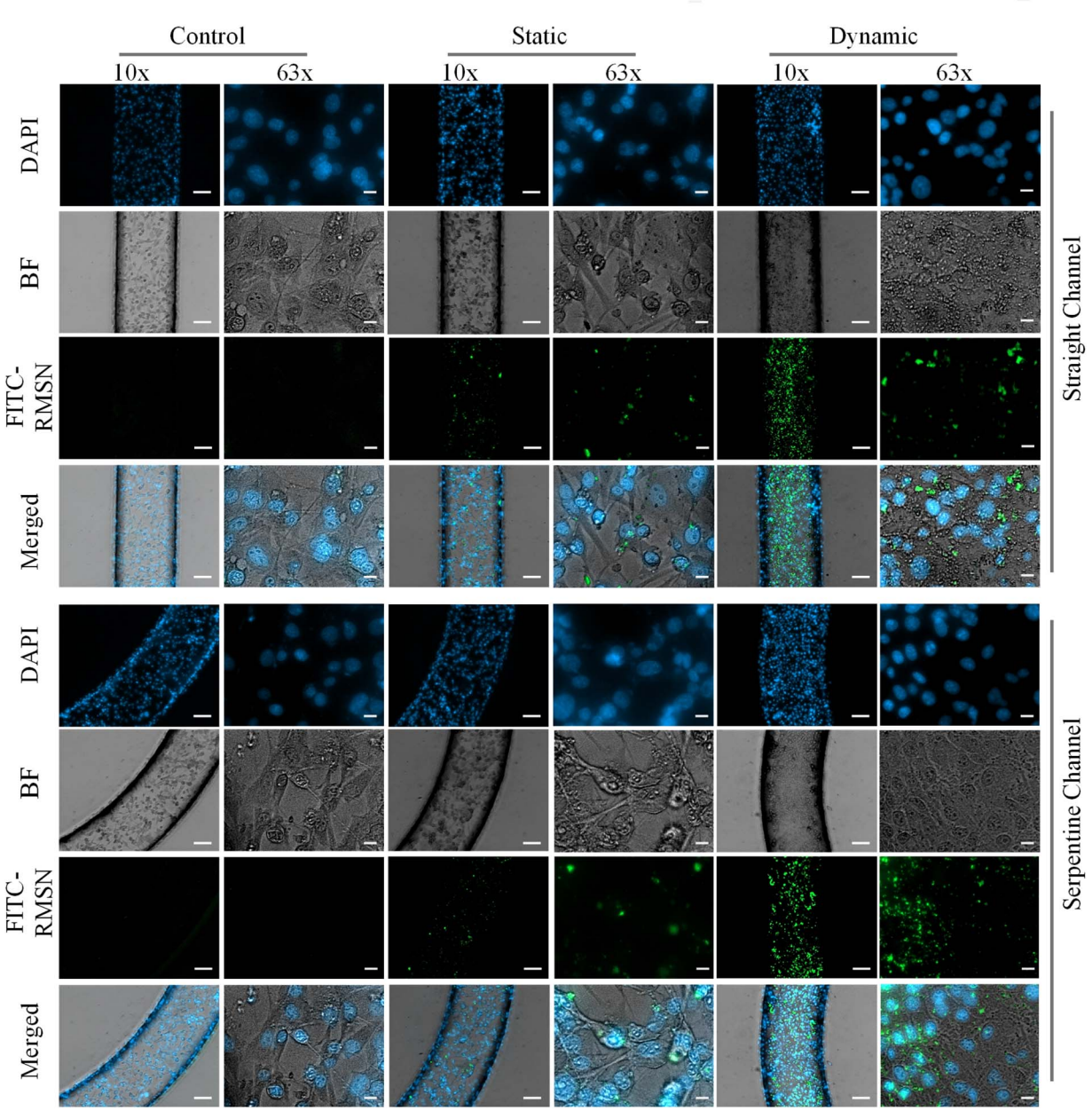

Fig. 8 Fluorescent images of U87 cells performed uptake assays with 100 μg mL^{-1} FITC-RMSN under static and dynamic flow conditions in straight and serpentine single-channel microfluidic chips. The flow rate in the dynamic mode was 60 μL h^{-1}. Cells nuclei were stained with DAPI, while Bright Field images were performed to show cells borders. Scale bars: 100 μm for the 10× images and 10 μm for the 63× images.

uptake in straight *versus* serpentine channel configurations showed no significant differences, suggesting that channel geometry (in at least this set-up) did not substantially influence nanoparticle internalization (Fig. 7C and 8).

Conclusion

The successful synthesis of MSNs using sustainable precursors highlights a promising approach to reducing environmental impact while generating materials with high surface area, tunable mesoporosity, and pH-responsive behavior suitable for biomedical applications. Importantly, the evaluation of these nanoparticles extended beyond their physicochemical characterization, incorporating advanced biological testing in a 3D microfluidic chip model.

A key insight from this work is the distinct difference in cellular uptake under static *versus* dynamic conditions. While static cultures led to limited penetration and peripheral accumulation, dynamic flow within the microfluidic chip promoted deeper internalization and more uniform distribution of nanoparticles across the cellular environment. These findings emphasize the importance of physiologically relevant models in predicting nanoparticle-cell interactions and suggest that

conventional 2D or static systems may not fully capture the therapeutic potential of nanocarriers.

Although the study provides strong proof of concept, there are areas that could be further improved in future work. For instance, incorporating a broader range of therapeutic agents would allow a more comprehensive evaluation of drug delivery potential. Extending the study to longer-term cytotoxicity assessments and *in vivo* validation would provide additional evidence of safety and translational relevance. Likewise, more detailed mechanistic studies on flow-enhanced uptake, such as the role of transport proteins or receptor-mediated pathways, could yield deeper biological insights. These refinements are not urgent concerns but represent natural next steps toward advancing this platform.

Taken together, this work highlights not only the potential of biowaste-derived MSNs as sustainable and versatile drug delivery platforms, but also the value of microfluidic models in mimicking physiological conditions. By integrating sustainable material design with advanced biological validation, the study lays the groundwork for next-generation nanomedicine systems that are environmentally responsible, clinically relevant, and scalable for real-world applications.

Author contributions

N. M. and S. P. conceptualized the study, developed the methodology; S. P. and G. B. performed the experiments, and analyzed the data; S. P. wrote the manuscript, which was reviewed by all authors. N. M. provided supervision on the experiments and analysis and edited the manuscript. All authors approved the final manuscript.

Conflicts of interest

The authors declare that they have no conflicts of interest that could influence the work reported in this paper.

Data availability

All data generated or analyzed during this study are included in this published article or are available from the corresponding author upon request.

Supplementary information is available. See DOI: **https://doi.org/10.1039/d5ra06132f**.

Acknowledgements

The authors would like to express their gratitude to the EMBO Installation Grant (Project No. IG-5352-2023, awarded to N. M.) and the ERC Starting Grant (Project No. 101116521 (MetaBrain), awarded to N. M.) for their financial support. This research was also supported by the Marie Skłodowska-Curie Actions (MSCA) postdoctoral fellowship (Project No. 101110722, awarded to S. P.). Additionally, G. B.'s fellowship was generously provided by the Faculty of Engineering and Natural Sciences at Sabancı University. We sincerely appreciate the generous support from these funding bodies, which made this work possible. The authors sincerely thank the Faculty of Engineering and Natural Sciences (FENS) at Sabancı University for providing materials and granting access to their facilities, as well as the Sabancı University Nanoscience Research and Application Center for access to TEM analysis. HDFs were gifted by Prof. Dr Tamer Onder's lab at Koç University, and HUVECs were provided by Dr Pelin Sağlam Metiner and Dr Ilgın Kımız Geboğlu at the Animal Cell Culture Laboratory of Ege University Bioengineering. U87 cells were gifted by Dr Gunes Esendagli's lab at Hacettepe University. We are grateful for their generous contributions.

References

1 Z.-A. Chen, *et al.*, Receptor ligand-free mesoporous silica nanoparticles: a streamlined strategy for targeted drug delivery across the blood–brain barrier, *ACS Nano*, 2024, **18**(20), 12716–12736.
2 D. M. Dereje, *et al.*, Squaraine-loaded mesoporous silica nanoparticles for antimicrobial Photodynamic Therapy against bacterial infection, *Microporous Mesoporous Mater.*, 2024, **372**, 113096.
3 S. Kesse, *et al.*, Mesoporous silica nanomaterials: versatile nanocarriers for cancer theranostics and drug and gene delivery, *Pharmaceutics*, 2019, **11**(2), 77.
4 D. Pakuła, B. Marciniec and R. E. Przekop, Direct synthesis of silicon compounds—From the beginning to green chemistry revolution, *AppliedChem*, 2023, **3**(1), 89–109.
5 S. Porrang, *et al.*, How advancing are mesoporous silica nanoparticles? A comprehensive review of the literature, *Int. J. Nanomed.*, 2022, 1803–1827.
6 S. Porrang, *et al.*, Preparation and in-vitro evaluation of mesoporous biogenic silica nanoparticles obtained from rice and wheat husk as a biocompatible carrier for anti-cancer drug delivery, *Eur. J. Pharm. Sci.*, 2021, **163**, 105866.
7 S. Porrang, *et al.*, Synthesis of temperature/pH dual-responsive mesoporous silica nanoparticles by surface modification and radical polymerization for anti-cancer drug delivery, *Colloids Surf., A*, 2021, **623**, 126719.
8 B. Xu, *et al.*, Multifunctional mesoporous silica nanoparticles for biomedical applications, *Signal Transduction Targeted Ther.*, 2023, **8**(1), 435.
9 B. Mayol, *et al.*, Self-propelled enzyme-controlled IR-mesoporous silica Janus nanomotor for smart delivery, *J. Colloid Interface Sci.*, 2024, **671**, 294–302.
10 S. Mohanan, *et al.*, Design and synthesis of cabazitaxel loaded core-shell mesoporous silica nanoparticles with different morphologies for prostate cancer therapy, *Small*, 2024, **20**(39), 2303269.
11 A. C. Ortiz, *et al.*, Release kinetics approach of stimuli-responsive mesoporous silica nanocarriers: pH-sensitive linker *versus* pH-sensitive framework, *J. Drug Delivery Sci. Technol.*, 2024, **91**, 105212.
12 X. Su, *et al.*, Pore engineering of micro/mesoporous nanomaterials for encapsulation, controlled release and variegated applications of essential oils, *J. Controlled Release*, 2024, **367**, 107–134.

13 R. Ciriminna, R. M. Laine and M. Pagliaro, Biobased silicon and biobased silica: two production routes whose time has come, *ChemSusChem*, 2023, **16**(19), e202300762.
14 Q. Alam, *et al.*, Novel low temperature synthesis of sodium silicate and ordered mesoporous silica from incineration bottom ash, *J. Cleaner Prod.*, 2019, **211**, 874–883.
15 A. L. Garcia, *et al.*, Synthesis of a green nano-silica material using beneficiated waste dunites and its application in concrete, *World J. Nano Sci. Eng.*, 2013, **2013**(3), 41–51.
16 I. J. Fernandes, *et al.*, Production and characterization of silica materials from rice husk ash by different combustion processes, *Powder Technol.*, 2024, **436**, 119473.
17 M. A. Khoj, Fabrication of silica/calcium alginate nanocomposite based on rice husk ash for efficient adsorption of phenol from water, *RSC Adv.*, 2024, **14**(33), 24322–24334.
18 D. Tharani and M. Ananthasubramanian, Influence of pre-treatment processes on the purity and characteristics of silica extracted from rice husk, *Biomass Convers. Biorefin.*, 2024, **14**(11), 12517–12529.
19 M. Ayaz, A. Shahbaz, M. Zahid, H. Ajaz, F. Saeed, U. B. Khalid, S Zahid and L. Liaqat, Green Synthesis Of Si-Nps From Rice And Wheat Husk And Their Applications In Nanocomposite Sheets, *Environ. Eng. Manage. J.*, 2023, **22**(3), 465–472.
20 S. Barani, *et al.*, Synthesis of silica nanoparticles (SiNPs) from agro-wastes for removal of heavy metals from an aqueous medium–a mini review, *Green Chem. Lett. Rev.*, 2024, **17**(1), 2422416.
21 K. Thilagham, *et al.*, Development of wheat husk biosilica and characterization of its areca reinforced polyester composite, *Biomass Convers. Biorefin.*, 2024, **14**(14), 15483–15492.
22 O. Mysiukiewicz, J. Szulc and A. Miklaszewski, The Influence of Horsetail (Equisetum arvense L.) Powder and Horsetail-Based Silica on the Crystallization Kinetics of Polylactide, *Materials*, 2024, **17**(23), 5697.
23 B. Saeed-Abadi, *et al.*, Effect of extraction solvent on silicon, isoquercitroside content, and antioxidant activity of common horsetail (Equisetum arvens L.) extract, *Biomass Convers. Biorefin.*, 2024, 1–8.
24 G. G. Lindner, *et al.*, Comparison of Biogenic Amorphous Silicas Found in Common Horsetail and Oat Husk With Synthetic Amorphous Silicas, *Front. Public Health*, 2022, **10**, 909196.
25 L. Zemnukhova, *et al.*, Properties of amorphous silica produced from rice and oat processing waste, *Inorg. Mater.*, 2006, **42**, 24–29.
26 L. A. September, *et al.*, Green synthesis of silica and silicon from agricultural residue sugarcane bagasse ash–a mini review, *RSC Adv.*, 2023, **13**(2), 1370–1380.
27 W. Xia and M. W. King, Advances in Targeted Delivery of Doxorubicin for Cancer Chemotherapy, *Bioengineering*, 2025, **12**(4), 430.
28 W. Zhang, *et al.*, Effects of morphology and size of nanoscale drug carriers on cellular uptake and internalization process: a review, *RSC Adv.*, 2023, **13**(1), 80–114.
29 J. D. L. Andrade, *et al.*, Rice husk-derived mesoporous silica as a promising platform for chemotherapeutic drug delivery, *Waste Biomass Valorization*, 2022, **13**(1), 241–254.
30 S. Y. Chen, J. Y. Jian and H. M. Lin, Functionalization of rice husk-derived mesoporous silica nanoparticles for targeted and imaging in cancer drug delivery, *J. Sci. Food Agric.*, 2024, **104**(4), 2120–2129.
31 X. Huang, *et al.*, The effect of the shape of mesoporous silica nanoparticles on cellular uptake and cell function, *Biomaterials*, 2010, **31**(3), 438–448.
32 W. Wang, *et al.*, Facile synthesis of uniform virus-like mesoporous silica nanoparticles for enhanced cellular internalization, *ACS Cent. Sci.*, 2017, **3**(8), 839–846.
33 S. Porrang, *et al.*, Direct surface modification of mesoporous silica nanoparticles by DBD plasma as a green approach to prepare dual-responsive drug delivery system, *J. Taiwan Inst. Chem. Eng.*, 2021, **123**, 47–58.
34 N. S. Zaharudin, *et al.*, Functionalized mesoporous silica nanoparticles templated by pyridinium ionic liquid for hydrophilic and hydrophobic drug release application, *J. Saudi Chem. Soc.*, 2020, **24**(3), 289–302.
35 H. I. Hussain, *et al.*, Mesoporous silica nanoparticles as a biomolecule delivery vehicle in plants, *J. Nanoparticle Res.*, 2013, **15**, 1–15.
36 B. Vinoda, *et al.*, Photocatalytic degradation of toxic methyl red dye using silica nanoparticles synthesized from rice husk ash, *J. Environ. Anal. Toxicol.*, 2015, **5**(6), 1000336.
37 D. Dorairaj, *et al.*, Green synthesis and characterization of UKMRC-8 rice husk-derived mesoporous silica nanoparticle for agricultural application, *Sci. Rep.*, 2022, **12**(1), 20162.
38 A. Owgi, *et al.*, The preferable Ni quantity to boost the performance of FSA for dry reforming of methane, *Fuel*, 2023, **332**, 126124.
39 S.-S. Wang, *et al.*, Amorphous silica-alumina composite with regulated acidity for efficient production of hydrogen *via* steam reforming of dimethyl ether, *Catal. Today*, 2020, **351**, 68–74.
40 N. Yalcin and V. Sevinc, Studies on silica obtained from rice husk, *Ceram. Int.*, 2001, **27**(2), 219–224.
41 L. A. Zemnukhova, *et al.*, Silicon-containing compounds in horsetail (Equisetum Equisetaceae) composition, *Appl. Chem. Biotechnol.*, 2019, **9**(29), 159–169.
42 M. Mundžić, *et al.*, Chlorotoxin-functionalized mesoporous silica nanoparticles for pH-responsive paclitaxel delivery to Glioblastoma multiforme, *Heliyon*, 2025, **11**(1), e41151.
43 F. Jiang, *et al.*, The controlling factors and prediction model of pore structure in global shale sediments based on random forest machine learning, *Earth-Sci. Rev.*, 2023, **241**, 104442.
44 F. J. Sotomayor, K. A. Cychosz and M. Thommes, Characterization of micro/mesoporous materials by physisorption: concepts and case studies, *Acc. Mater. Surf. Res*, 2018, **3**(2), 34–50.
45 C. Keluo, *et al.*, Model construction of micro-pores in shale: A case study of Silurian Longmaxi Formation shale in Dianqianbei area, SW China, *Pet. Explor. Dev.*, 2018, **45**(3), 412–421.

46 A. H. Khalbas, *et al.*, Drug loading methods and kinetic release models using of mesoporous silica nanoparticles as a drug delivery system: A review, *S. Afr. J. Chem. Eng.*, 2024, 261–280.
47 M. Hosonuma and K. Yoshimura, Association between pH regulation of the tumor microenvironment and immunological state, *Front. Oncol.*, 2023, **13**, 1175563.
48 E. S. Lee, *et al.*, Tumor pH-responsive flower-like micelles of poly (L-lactic acid)-b-poly (ethylene glycol)-b-poly (L-histidine), *J. Controlled Release*, 2007, **123**(1), 19–26.
49 K. Huang, *et al.*, Targeted delivery and release of doxorubicin using a pH-responsive and self-assembling copolymer, *J. Mater. Chem. B*, 2017, **5**(31), 6356–6365.
50 E. B. Manaia, *et al.*, Physicochemical characterization of drug nanocarriers, *Int. J. Nanomed.*, 2017, 4991–5011.
51 A. U. Rehman, *et al.*, Development of doxorubicin hydrochloride loaded pH-sensitive liposomes: Investigation on the impact of chemical nature of lipids and liposome composition on pH-sensitivity, *Eur. J. Pharm. Biopharm.*, 2018, **133**, 331–338.
52 T. Dos Santos, *et al.*, Quantitative assessment of the comparative nanoparticle-uptake efficiency of a range of cell lines, *Small*, 2011, **7**(23), 3341–3349.
53 A. Sohrabi Kashani and M. Packirisamy, Cancer-nano-interaction: From cellular uptake to mechanobiological responses, *Int. J. Mol. Sci.*, 2021, **22**(17), 9587.
54 Y. Goldstein, *et al.*, Particle uptake in cancer cells can predict malignancy and drug resistance using machine learning, *Sci. Adv.*, 2024, **10**(22), eadj4370.
55 M. Ekkapongpisit, *et al.*, Biocompatibility, endocytosis, and intracellular trafficking of mesoporous silica and polystyrene nanoparticles in ovarian cancer cells: effects of size and surface charge groups, *Int. J. Nanomed.*, 2012, 4147–4158.
56 Y. Zhou, *et al.*, Mesoporous silica nanoparticles for drug and gene delivery, *Acta Pharm. Sin. B*, 2018, **8**(2), 165–177.